Power laws for the thermal slip length of a liquid/solid interface from the structure and frequency response of the contact zone

Hiroki Kaifu and Sandra M. Troian*

California Institute of Technology, Thomas J. Watson, Sr., Laboratories of Applied Physics, Pasadena, California 91125, USA

(Received 16 October 2024; revised 26 November 2025; accepted 18 December 2025; published 26 January 2026)

The newest and most powerful electronic chips for applications such as artificial intelligence generate so much heat that liquid-based cooling has become indispensable to prevent breakdown from thermal runaway effects. While cooling schemes such as microfluidic networks or liquid immersion are proving effective for now, further progress requires tackling an age-old problem—namely, the intrinsic thermal impedance of the liquid/solid (L/S) interface, quantified either by the thermal boundary resistance or by the thermal slip length. While there are well-known models for estimating bounds on the thermal impedance of a superfluid/metal interface, no analytic models or experimental data are available for normal liquid/solid interfaces. Researchers therefore rely on nonequilibrium molecular dynamics simulations to gain insight into phonon transfer at the L/S interface. Here we explore correlated order and motion within the L/S contact zone in an effort to extract general scaling relations for the thermal slip length in Lennard-Jones (LJ) systems. We focus on the in-plane structure factor and dominant vibrational frequency of the first solid and liquid layer for 180 systems. When scaled by the temperature of the liquid contact layer and characteristic LJ interaction distance, the data collapse onto two power-law equations, one quantifying the reduction in thermal impedance from enhanced in-plane translational order and the other from enhanced frequency matching in the contact zone. More generally, these power-law relations highlight the critical role of surface acoustic phonons, an area of focus that may also prove useful to the development of analytic models as well as instrumentation for testing the relations proposed.

DOI: 10.1103/ztng-519w

I. INTRODUCTION

High-performance CPUs and graphics-processing units for power-intensive applications such as artificial intelligence and cryptocurrency exchange generate such tremendous heat within such small volumes that chip designers have had to pivot from air to liquid cooling to prevent failure from thermal runaway and consequent deleterious behavior [1–3]. Liquid cooling has also demonstrated faster clock speeds, higher efficiency, improved performance, and better stability in systems ranging from conventional complementary metal-oxide semiconductor and superconducting processors to solid-state quantum devices [4]. While use of aqueous liquids is still common, liquid metals and alloys are of growing interest because of their superior thermophysical and other properties, such as high thermal and electrical conductivity, high boiling point, high surface tension, and low viscosity [5]. Metallic-based liquids can also be transported throughout electronic devices with the use of compact magnetofluid dynamic pumps, which are vibration-free and therefore operate quietly and efficiently.

Cooling schemes using two-phase cooling in microfluidic networks or direct liquid immersion are currently in use and being refined. However, further progress requires tackling the age-old problem of the intrinsic thermal impedance of any liquid/solid (L/S) interface due to the discontinuity in material properties at the boundary. This impedance is typically quantified by the magnitude of the thermal boundary resistance or the thermal slip length. The latter quantity is the preferred measure in this study to draw an analogy with the velocity slip length in hydrodynamic systems. Illustrated in Fig. 1 is the thermal slip length of a L/S interface for a constant thermal flux J_z propagating in the direction normal to the interface, here oriented along

*Contact author: stroian@caltech.edu, http://www.troian.caltech.edu/

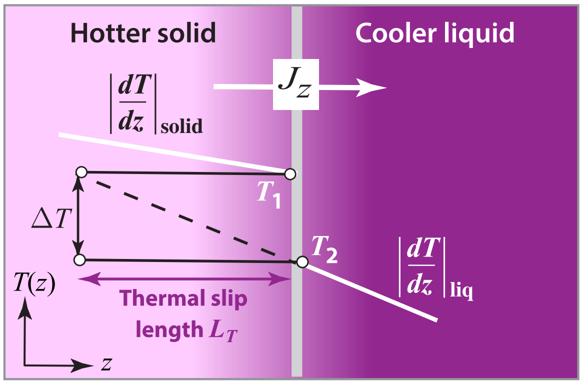

FIG. 1. Illustration of the thermal slip length.

the $\hat{z}$ axis. It is defined by the relation

$$L_T = \frac{\Delta T}{|dT/dz|_{\text{liq}}}, \tag{1}$$

where $|dT/dz|_{\text{liq}}$ is the magnitude of the thermal gradient in the liquid interior, which in this study reduces to a constant that depends on the input variables due to the linearity of the temperature profile. While in macroscopic L/S systems the thermal impedance of the interface is far smaller than that of the bulk liquid and solid layers and therefore negligible, that is not the case in microscale or nanoscale systems, which manifest very large surface-to-volume ratios.

Equation (1) is just a definition, of course, since all the dependencies and complexities of a given system are buried in the variables ΔT and J_z. Despite decades of effort, the only L/S systems for which there exist predictive models for estimating the thermal boundary impedance are those pertaining to superfluid helium/metal interfaces. On the experimental side, superfluid/metal systems have special properties that allow accurate measurement of variables such as temperature, pressure, elastic properties of the solid and 1iquid and the excitation spectrum of phonons in the bulk and at the interface. Even so, the two best known analytic relations for such systems provide bounds only on the magnitude of the thermal boundary resistance (i.e., Kapitza resistance), depending on whether phonon behavior at the interface is predominantly specular or diffusive [6–8]. There are no such equations for normal L/S systems (i.e., those not involving superfluids).

This situation poses a serious problem on a fundamental level when one is trying to solve for the temperature distribution throughout a L/S system on the basis of the differential equations governing thermal transfer. At macroscopic scales, since the interface boundary resistance is relatively negligible, $\Delta T = T_1 - T_2 \approx 0$, such that the temperature of the solid surface is practically identical to that of the first liquid monolayer in contact with the substrate—which in this study is called the "contact layer." In microscale or nanoscale systems however, the boundary values T_1 and T_2 are unknown and the difference typically not negligible. Furthermore, this dilemma cannot be resolved by appealing to experimental data since, aside from the special class of systems mentioned above, there are no adequate experimental probes for measuring ΔT in normal L/S systems.

A. Analogy with velocity slip length at a L/S interface

There is an analogous dilemma in hydrodynamic systems involving velocity slip at the interface of a liquid and solid in relative motion. Until recently, the velocity boundary condition needed to solve Cauchy's equation of motion was based on a phenomenological relation known as the "Navier slip law" [9], wherein the velocity slip length is treated as an unknown constant. Unlike other boundary conditions needed to solve the governing equations for mass, momentum, and energy transport, the thermal slip and velocity slip boundary conditions are unique in that they cannot be deduced from conservation laws or considerations of symmetry. For this reason, researchers in both fields have come to rely heavily on nonequilibrium molecular dynamics (NEMD) simulations to uncover correlations among the many system variables and the corresponding slip lengths.

During the past several decades, advances in NEMD simulations have helped reveal many aspects of velocity slip in systems ranging from simple liquids or polymeric fluids to more complex fluids flowing across the surface of smooth or rough, wetting or nonwetting, chemically patterned or textured substrates. An early study revealed that when normalized by key asymptotic variables, the velocity slip length exhibits a distinctive power-law dependence on the liquid shear rate [10]. That boundary condition has been adopted extensively and further generalized to describe many different systems. Lesser known or emphasized, but equally important, is the fact that the velocity slip length exhibits a strong inverse dependence on the peak value of the in-plane structure factor of the contact layer. This dependence, which hinges on the degree of translational order within the contact layer induced by the substrate potential, has since been verified in many simulations and even validated by analytic models for certain systems [11–15].

B. Relevant prior studies and open questions

The phenomenon of thermal slip at a normal L/S interface has also been investigated extensively by NEMD simulations, which have revealed the influence of system properties such as the wettability of the L/S interface [16–21], the pressure of the bulk liquid against the solid surface [22,23], the temperature of the solid surface [24, 25], the solid surface roughness [21], the symmetry of the solid lattice [26–28], the thickness of the liquid layer between two solid lattices at different temperatures [29], and the width of the L/S density depletion zone [30–32]. However, no general relations for predicting the overall magnitude of the thermal slip length have been developed, in part because of the difficulty in untangling effects arising from poorly understood interactions among the various system parameters. In this study, we therefore adopt a different approach by focusing on two key measures of *correlated behavior* within the L/S contact zone, defined as the interfacial region spanning the first solid layer and the first liquid layer, i.e., contact layer. These two measures, corresponding to the structural order and the dominant vibrational frequency of the contact layer, reveal the influence of the solid substrate potential on the transmission of acoustic phonons across the L/S boundary.

C. Choice of intermolecular potential in NEMD simulations

The overwhelming majority of computational studies on thermal transport across a L/S interface have used the 12-6 Lennard-Jones (LJ) pair potential, which for decades has served as the canonical reference for investigation of physical mechanisms in the presence of statistical fluctuations. The LJ potential offers a simple, yet accurate description of the balance between attractive and repulsive interactions between neutral particles (i.e., molecules or molecular units with closed electron shells). This potential, now regarded as the archetype model for efficient and realistic simulations, is also often used as the building block for more complex substances involving bonded interactions. For simple metallic systems such as face-centered-cubic (fcc) metal interfaces, the LJ potential is capable of generating highly accurate material constants with far less computational effort than embedded-atom potentials or density functional calculations [33,34].

A key feature of the LJ potential is its general form given by $U = \varepsilon\,\mathcal{U}(r/\sigma)$, where ε and σ specify characteristic energy and distance scales and $\mathcal{U}$ denotes a universal function of the scaled spatial coordinate r/σ. According to the law of corresponding states [35], transport coefficients, including the thermal diffusivity, molecular diffusivity and kinematic viscosity, can be directly mapped from one system to another by simple rescaling of the constants ε and σ. For this reason, while many studies, including ours, are based on the scales and properties of argon, the results are more generally applicable.

D. Motivation for the current study

In a recent study [28], we demonstrated a strong correspondence between the magnitude of the thermal slip length and the motion of liquid particles in the contact layer. In particular, those simulations revealed how the depth and width of the corrugation of the L/S periodic surface potential control the degree of particle localization by repressing in-plane migration and diffusion. We coined that behavior "two-dimensional (2D) caging" in reference to the well-known three-dimensional (3D) caging phenomena leading to glassy behavior in amorphous systems. There we showed that 2D caging enhances thermal transfer out of the plane between liquid layers, thereby reducing the thermal slip length. Informed by those findings, we wanted to explore the process in more detail by examining the relation between the thermal slip length and two important measures of the L/S contact zone as quantified by the structural and vibrational characteristics of the contact layer. The results we report here, based on analysis of 180 different L/S systems interacting via LJ potentials, demonstrate the existence of distinct power-law relations for the thermal slip length described in the spatial and frequency domains.

II. COMPUTATIONAL DETAILS

In this section we outline details of the NEMD simulations using the open-source package LAMMPS, a flexible tool for particle-based simulations of gases, liquids, and solids in systems ranging from atomic to macroscopic length scales [36,37]. Additional details pertaining to these simulations can be found in Ref. [28].

A. Model geometry and interaction potentials

The simulations conducted were based on the rectangular layered structure shown in Fig. 2 describing a quiescent liquid layer sandwiched between two identical crystalline solids modeled by fcc lattices. Each solid was maintained

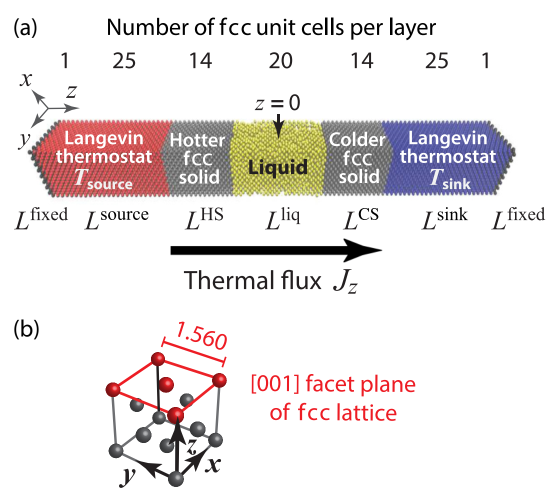

FIG. 2. (a) Layered geometry of the entire computational cell. Scalings of variables and layer dimensions for the geometry can be found in Tables I and II. The coordinate origin $z = 0$ was situated at the midplane of the liquid layer. (b) fcc crystal unit cell with lattice constant 1.560 (reduced units) showing the [001] facet plane (red). For all runs, the surface normal to the [001] plane was oriented parallel to the direction of the thermal flux J_z.

TABLE I. Quantities, symbols, and numerical values used to rescale variables based on the elemental fluid argon [38–40]. Boltzmann's constant $k_B = 1.380649 \times 10^{-23}$ J/K.

Physical quantity	Symbol and numerical value
Mass[a]	$m = 6.690 \times 10^{-26}$ kg
Length[a]	$\sigma = 0.3405 \times 10^{-9}$ m
Energy[a]	$\epsilon = 165.3 \times 10^{-23}$ J
Temperature[a]	$T = \epsilon/k_B = 119.8$ K
Time[a]	$t = (m\sigma^2/\epsilon)^{1/2} = 2.14$ ps
Mass density[a]	$\rho = m/\sigma^3$
Pressure[a]	$p = \epsilon/\sigma^3 = 0.4187$ MPa
Effective particle diameter[a]	$\sigma_{LL} = \sigma_{SS} = \sigma$
	$\sigma_{LS} = 0.8\sigma$, 1.0σ, or 1.2σ
fcc edge length[a]	$a = 1.560\sigma = 5.312 \times 10^{-10}$ m
Interaction energy[a]	$\epsilon_{LL} = \epsilon$
	$\epsilon_{LS} = (0.1\text{–}1.0)\epsilon$
	$\epsilon_{SS} = 10\epsilon$
Scaled variable	**Value in scaled units**
Solid and liquid particle mass	1.0
LJ repulsive distance	$\sigma_{LL} = \sigma_{SS} = 1.0$
	$\sigma_{LS} = 0.8, 1.0,$ or 1.2
fcc edge length	$a = 1.560$
Integration time step	$\Delta t_{\text{int}} = 0.002$
Thermostat setting	$(T_{\text{source}}, T_{\text{sink}}) =$
	$(1.8, 0.8), (1.6, 1.0),$ or $(1.4, 1.2)$
LJ interaction energy	$\varepsilon_{LL} = 1.0$
	$\varepsilon_{LS} = 0.1, 0.2, \ldots, 0.9, 1.0$
	$\varepsilon_{SS} = 10$
Bulk liquid density	$\rho_L \approx 0.84$
fcc unit cell density	$\rho_S = 1.0536$

[a]Dimensional quantity.

TABLE II. Dimensions of the layered system in Fig. 2 in reduced units.

L_x	12.48
L_y	12.48
L^{fixed} (one unit cell per end)	1.56
L^{source}	39.00
L^{HS}	21.84
L^{liq}	31.20
L^{CS}	21.84
L^{sink}	39.00
Total length along z axis	156.00

at a constant temperature by direct thermal contact with another fcc lattice acting as a Langevin thermostat. The left thermostat was set to temperature T_{source} and the right one was set to T_{sink}, which naturally generated a constant thermal flux along the $\hat{z}$ axis. Particles in the outermost layer at each end of the cell were fixed in place to prevent sublimation. All solid lattices were oriented with their [001] facet plane parallel to the L/S interface. Since the mass of all liquid and solid particles was set equal to 1 (in reduced units), the mass density equaled the number density. Periodic boundary conditions were enforced along the $\hat{x}$ and $\hat{y}$ axes.

All particles were made to interact via a truncated and shifted LJ potential given by

$$U_{\text{LJTS}}(r_{ij}) = \begin{cases} U(r_{ij}) - U(r_c) & \text{if } r_{ij} \le r_c, \\ 0 & \text{if } r_{ij} > r_c, \end{cases} \tag{2}$$

where

$$U(r_{ij}) = 4\varepsilon_{ij}\left[\left(\frac{\sigma_{ij}}{r_{ij}}\right)^{12} - \left(\frac{\sigma_{ij}}{r_{ij}}\right)^{6}\right]. \tag{3}$$

This form ensures no discontinuity in the intermolecular force despite the interaction cutoff radius r_c. Here, subscripts ij denote pairwise-interacting particles $i/j =$ L/L, S/S, or L/S, $r_{ij} = |\mathbf{r}_i - \mathbf{r}_j|$ is the pairwise separation distance between particle i and particle j, ε_{ij} is the pairwise interaction energy, and σ_{ij} is the pairwise distance, where $U(r = \sigma_{ij}) = 0$, also called the "effective particle diameter."

The input parameters for each run were $(T_{\text{source}}, T_{\text{sink}})$, σ_{LS}, and ε_{LS}, the latter range spanning the so-called nonwetting-to-wetting regimes. The specific choice of pair values $(T_{\text{source}}, T_{\text{sink}})$ ensured not only that the interior of the liquid layer in all runs remained far from any critical or triple point [40,41] but also that it remained close to the average temperature $(T_{\text{source}} + T_{\text{sink}})/2 = 1.3$ and average density $\rho_{\text{bulk}} \approx 0.84$. The computational cell was designed with a relatively large liquid layer. Simultaneous measurements at the hotter and colder sides therefore helped reveal the influence of contact layer temperature T_c. In total, the geometry helped generate 180 L/S interfaces for analysis.

Most NEMD studies in this field report that the crystalline solids are constructed with the use of a harmonic wall-spring model in which particles are closely tethered to sites of a periodic lattice with the use of a Hookean spring force [29,37,42]. Depending on the temperature range and other input variables, this type of construction can dampen or altogether eliminate anharmonic phonons. To prevent this, the particles in the solid layers in this study were made to interact via a strong-binding LJ potential [43–46] with $\varepsilon_{SS} = 10$ and $\sigma_{SS} = 1.0$, while the liquid/liquid interaction constants were set to $\varepsilon_{LL} = 1.0$ and $\sigma_{LL} = 1.0$. Since the melting temperature of a LJ solid can be estimated from the relation $T_m \approx \varepsilon_{SS}/2$ [47], $\varepsilon_{SS} = 10$ ensured that the crystal remained in the solid state for the temperatures generated in this study. Simulations at isothermal conditions for modeling simple fcc metals have shown that similar choices of intermolecular constants yield accurate material property values [33,34].

The thickness of the two lattices acting as Langevin thermostats was also chosen to exceed that of the unconstrained solid layers in order to avoid spurious reductions in thermal boundary resistance [23]. Studies have shown [23,48] that when the phonon mean free path in the thermal reservoir region satisfies the relation $\Lambda = c_l \times \tau_{\text{damp}} \leq 2L$, where c_l is the speed of longitudinal sound waves, L is the reservoir layer thickness, and τ_{damp} is the Langevin damping constant, phonons are dissipated before undergoing reflections from the exterior boundary toward the L/S interface. For an fcc crystal, c_l was estimated from the relation [47] $c_l = 9.53\sqrt{\varepsilon_{SS}}$. Therefore, for the parameters in our study—namely, $\tau_{\text{damp}} = 1$ and $L_s = L^{\text{source}} = L^{\text{sink}} = 39$—the inequality $\Lambda = c_l \times \tau_{\text{damp}} = 9.53\sqrt{10} \approx 30 \leq 2L_s = 78$ was well-satisfied.

B. Thermal flux regulation

The solid/liquid/solid (S/L/S) layers were first thermally equilibrated with the use of a canonical ensemble (constant NVT conditions) at temperature $T = 1.3$ with the use of a Nosé-Hoover thermostat [49] for a time $t_{\text{eq}} = 10^5\Delta t_{\text{int}} = 200$. That thermostat was then turned off, and a Langevin thermostat [50] was applied to particles in the two solid layers acting as the thermal source and sink to maintain each layer at a different fixed temperature T_s by enforcing the Langevin equation (reduced units)

$$\frac{d^2\mathbf{r}_i}{dt^2} = -\sum_{i\neq j} \nabla U_{\text{LJST}} \cdot \mathbf{r}_{ij} - \frac{1}{\tau_{\text{damp}}}\frac{d\mathbf{r}_i}{dt} + \mathbf{F}_{\text{stoch}}. \tag{4}$$

We chose the damping constant $\tau_{\text{damp}} = 500\Delta t_{\text{int}} = 1.0$, and the magnitude of the normally distributed random force F_{stoch} was set to the value $[T_s/(\tau_{\text{damp}}\Delta t_{\text{int}})]^{1/2}$. The entire system was then stabilized for an additional period of $2 \times 10^5\Delta t_{\text{int}} = 400$ to ensure a steady uniform thermal flux propagated across the S/L/S system. Measurements of various properties were then extracted from particle trajectories following Newton's equation with the use of second-order Verlet integration [39] with time step $\Delta t_{\text{int}} = 0.002$.

The thermal flux across the system was extracted from the relation

$$J_z = \frac{1}{L_x \times L_y}\left\langle \frac{E_{\text{net}}(t)}{t} \right\rangle, \tag{5}$$

where $E_{\text{net}}(t)$ is the net energy input during the interval t required to maintain the set-point values $(T_{\text{source}}, T_{\text{sink}})$. Angular brackets here and elsewhere denote ensemble averaging as described below. It was found that $\langle E_{\text{net}}(t)\rangle$ increased linearly in time, indicating that a constant thermal flux had been established. The mean and standard deviation of the thermal gradient $|dT/dz|$ within the bulk of the liquid and solid regions were extracted from linear least squares fits.

It has been reported that application of high pressure to a liquid can lead to a threefold-to-fourfold reduction in the thermal impedance of the L/S interface [23], stemming from ultradense packing of particles against the solid wall. To eliminate this effect from our study, we checked the typical magnitudes of the virial and kinetic contributions to the pressure p in the liquid interior. As an example, for $(T_{\text{source}}, T_{\text{sink}}) = (1.6, 1, 0)$ and $\sigma_{LS} = 1.0$, the virial contribution for $\varepsilon_{LS} = 0.1$ was $p = 2.72 \pm 0.03$ and for $\varepsilon_{LS} = 1.0$ was $p = 2.54 \pm 0.02$. The kinetic contribution to the pressure $p = 1.5$ remained constant for all runs since the average temperature in the liquid interior was designed to remain near $T = 1.3$. The total pressure within the liquid interior was found always to be in the low single digits, far smaller than the pressures needed to induce a sizeable reduction in thermal impedance from packing effects alone.

C. Measurements extracted

The geometry in Fig. 2 allowed simultaneous measurement of various quantities from the hotter and colder sides of the liquid layer while subject to the same thermal flux. In this study, key measurements extracted from the hotter and colder interfaces included the temperature T_c and peak density ρ_c of the contact layer, the width of the liquid density depletion layer δ_{LS} (i.e., the separation distance between the peak density of the contact layer and the peak density of the first solid layer), the thermal gradient within the interior of the liquid and solid layers, the temperature drop ΔT across the L/S interface, the thermal slip length L_T, the maximum value of the in-plane static structure factor of the contact layer $S^{\parallel}_{\max}$, and the frequencies ν_S and ν_L corresponding to the peak values in the phonon density of states for the first solid layer and the contact (liquid) layer.

1. Ensemble averaging of stationary quantities

After a constant thermal flux had been established, trajectory data were sampled at intervals of $500\Delta t_{\text{int}} = 1.0$ for total period $t_{\text{total}} = 5 \times 10^6\Delta t_{\text{int}} = 10^4$. The sampling interval equaled the approximate decay interval of the velocity autocorrelation function of particles in the contact layer. These data strings were divided into ten nonoverlapping segments for ensemble averaging.

The density and temperature distributions along the $\hat{z}$ axis were obtained by division of the S/L/S partitions into nonoverlapping bins of volume $L_x \times L_y \times \Delta z_{\text{bin}}$. A slender bin width Δz_{bin} of 0.016 was used to capture fine details of the oscillations in the liquid layer near solid surfaces. The average density in each bin was estimated as $\rho_{\text{bin}} = \langle N_{\text{bin}}\rangle/V_{\text{bin}}$, where N_{bin} represents the average number of particles in a bin. The thickness of the contact layer was defined to be the distance separating the adjacent minima of the first and always largest oscillation in the liquid density profile near the solid surface; the peak value of the first oscillation is denoted ρ_c. It was found that the speed of particles in both the contact layer and the first solid layer conformed to a Maxwell-Boltzmann distribution, thereby reflecting a state of *local thermal equilibrium*. The average temperature in each bin (based on bin width $\Delta z_{\rm bin} = 0.785$) was therefore computed from the equipartition relation

$$T_{\rm bin} = \left\langle \frac{1}{3N_{\rm bin}} \sum_i^{N_{\rm bin}} \mathbf{v}_i^2 \right\rangle, \tag{6}$$

where $\mathbf{v}_i$ denotes the 3D velocity vector of particle i.

The temperature drop across the L/S interface was obtained by extrapolation of the linear temperature profile (confirming thermal conduction) within the solid and liquid layers toward the L/S interface. ΔT represents the temperature drop at the midpoint of the distance separating the peaks in density of the first solid layer and the contact layer. This separation distance is also sometimes called the "depletion layer thickness" δ_{LS}. The thermal slip length was then obtained from the relation

$$L_T = \left\langle \frac{\Delta T}{|dT/dz|_{\rm liq}} \right\rangle. \tag{7}$$

The degree of long-range translational order within the contact layer was quantified by the in-plane static structure factor [51]

$$S_c^{\parallel}(\mathbf{k}) = \left\langle \frac{1}{N_c^2} \sum_{p=1}^{N_c} \sum_{q=1}^{N_c} \exp\left[i\mathbf{k}\cdot(\mathbf{r}_p - \mathbf{r}_q)\right] \right\rangle, \tag{8}$$

where $\parallel$ signifies the planar coordinates $\mathbf{r} = (x, y)$ and wave numbers $\mathbf{k} = (k_x, k_y)$ for the total number of particles in the layer N_c. Equation (8) was normalized to span the range $0 \le S_c^{\parallel}(\mathbf{k}) \le 1$. We found that the global maximum of Eq. (8), denoted by $S_{\rm max}^{\parallel}$, always coincided with the set of smallest reciprocal lattice vectors of the [001] facet plane of the fcc solid lattices.

2. Ensemble averaging of time-dependent quantities

Measurements of the velocity autocorrelation function were collected over a total period $t_{\rm total} = 1.5 \times 10^6 \Delta t_{\rm int} = 3 \times 10^3$, and were then divided into three nonoverlapping equal time blocks with initial times $t_o^B = 0$, $t_o^B = 10^3$, and $t_o^B = 2 \times 10^3$. Velocities in each block were sampled at intervals of $10 \times \Delta t_{\rm int} = 0.02$, which generated a sequence of autocorrelation values spanning the interval $t_f - t_o$ for $t_o = t_o^B + (0, 10, 20, \ldots, 475\,000) \times 0.02$. Since particles in the first solid layer remained in that layer throughout, the final sampling time t_f was set to 50. Since particles in the contact layer could exit and reenter that layer, a different strategy was needed to establish an appropriate interval for evaluating correlations. Autocorrelation data were therefore restricted to that subset of particles in the contact layer $N_c(t_o, t_f) \ge 10$, found to remain in that layer throughout the interval $t_f - t_o$. In all cases, we ensured that this interval exceeded the velocity autocorrelation decay time by at least an order of magnitude.

The phonon density of states per particle $\mathcal{D}(\nu)$, representing the spectrum of normal mode vibrations, was computed from the relation [52,53]

$$\mathcal{D}(\nu) = \left\langle \frac{4}{N_L T_L} \int_0^{t_f} \sum_{j=1}^{N_L} \mathbf{v}_j(t_o + t)\cdot \mathbf{v}_j(t_o) \cos(2\pi\nu t)\, dt \right\rangle_{t_o}^{B}, \tag{9}$$

where N_L and T_L refer to the number of particles and the temperature of the first solid layer or contact layer, as appropriate. Equation (9) was normalized to satisfy the equipartition relation $\int_0^\infty \mathcal{D}(\nu)\, d\nu = 3$, reflecting 3 degrees of freedom for vibrational motion. Since different initial times t_o led to different final times t_f, the smallest value of t_f within each time block was used to estimate the mean value for that block. The smallest value of t_f of all three blocks was then used to compute the final block average for $\mathcal{D}(\nu)$. The notation $\langle\cdot\rangle_{t_o}^B$ signifies the ensemble average over initial times t_o followed by the three-block average.

III. SIMULATION RESULTS

A. Behavior of thermal flux J_z

Figure 3 shows the increase in thermal flux J_z across the S/L/S system for increasing values of $T_{\rm source} - T_{\rm sink}$ and ε_{LS} and decreasing values of σ_{LS}. For constant ε_{LS}, the highest thermal flux is achieved with the largest differential $T_{\rm source} - T_{\rm sink}$ and smallest value of σ_{LS}. For the smallest applied differential (1.4, 1.2), J_z is relatively insensitive to σ_{LS} and far less sensitive to ε_{LS}. Overall, the larger the differential $T_{\rm source} - T_{\rm sink}$, the stronger the influence of ε_{LS} and σ_{LS} on the thermal flux.

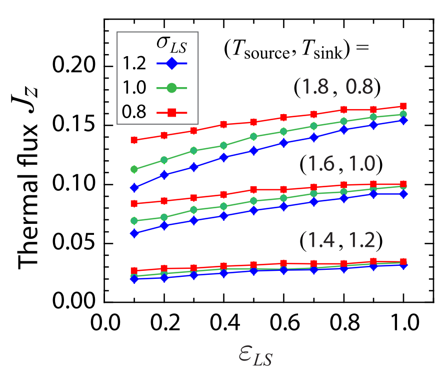

FIG. 3. Increase in thermal flux J_z with increasing $T_{\rm source} - T_{\rm sink}$, increasing ε_{LS}, and decreasing σ_{LS}. Connector lines are a guide for the eye.

B. Behavior of temperature jump ΔT

Figure 4 shows the reduction in the temperature jump ΔT at the hotter and colder L/S interfaces for decreasing differential $T_{\mathrm{source}} - T_{\mathrm{sink}}$, decreasing σ_{LS}, and increasing ε_{LS}. Further inspection of the data in Fig. 4 reveals some unexpected features. (The tabulated entries in Ref. [54] evidence the trends reported below in more detail.) For example, when $\sigma_{LS} = 1.2$, the temperature drop at the colder L/S interface is always larger than that at the hotter interface irrespective of the value of ε_{LS}. However, the opposite behavior is observed for $\sigma_{LS} = 0.8$, as is clear from Figs. 4(a) and 4(b). For the systems in Fig. 4(c), the tabulated entries in Ref. [54] confirm that the behavior reverts to larger thermal jumps at the colder interface. For the intermediate case $\sigma_{LS} = 1.0$, the thermal jump at the colder side can be larger or smaller that at the hotter side depending on the value of ε_{LS}; this transition occurs near $\varepsilon_{LS} = 0.6$. Another interesting observation is that the smallest overall temperature drop occurs at the hotter interface for $(T_{\mathrm{source}}, T_{\mathrm{sink}}) = (1.4, 1.2)$, $\sigma_{LS} = 0.8$, and $\varepsilon_{LS} = 1.0$. On the basis of considerations of kinetic energy and collision frequency between liquid and solid particles, one might have expected the smallest temperature drops in the hottest layers generated with the setting $T_{\mathrm{source}} = 1.8$, but that is not the case. This illustrates that ΔT is influenced by a number of variables, including T_{source}, T_{sink}, ε_{LS}, and σ_{LS}, and so its behavior cannot necessarily be intuited *a priori*.

This introduces another misconception that occasionally creeps into the literature—namely, that the higher the contact density ρ_c, the smaller must be the temperature drop ΔT because of the more numerous L/S collisions per unit area [55,56]. The data in Ref. [54] confirm that for certain values of $(T_{\mathrm{source}}, T_{\mathrm{sink}})$ and σ_{LS}, an increase in ε_{LS} does cause an increase in ρ_c and a decrease in ΔT. However, the data in Fig. 4 show that when ε_{LS} is held constant and σ_{LS} is allowed to increase, then an increase in ρ_c leads to an increase in ΔT, a trend noted previously [28]. The reason for this is that at constant $(T_{\mathrm{source}}, T_{\mathrm{sink}})$ and ε_{LS}, larger

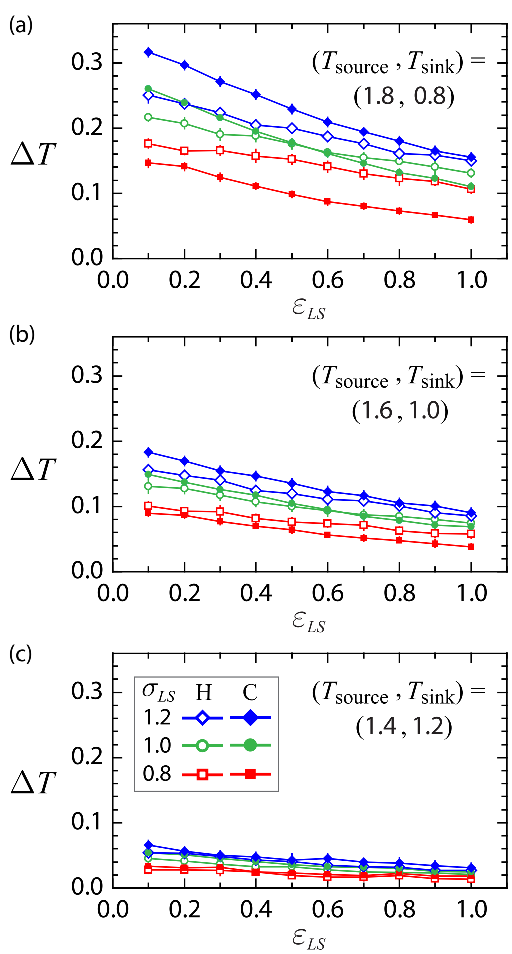

FIG. 4. (a)–(c) Reduction in the temperature jump ΔT at the hotter (H) and colder (C) L/S interfaces for decreasing differential temperature $T_{\mathrm{source}} - T_{\mathrm{sink}}$, decreasing σ_{LS}, and increasing ε_{LS}. Connector lines are a guide for the eye.

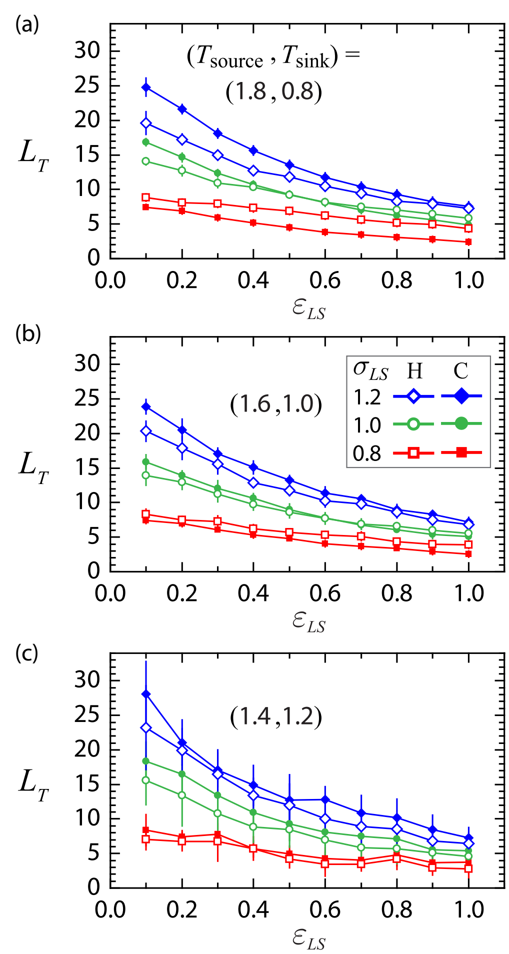

FIG. 5. (a)–(c) Reduction in the thermal slip length L_T at the hotter (H) and colder (C) L/S interfaces with increasing ε_{LS} and decreasing σ_{LS}.

values of σ_{LS} lead to greater depletion layer thicknesses δ_{LS}. Since this depletion zone acts as a thermal insulation layer, the wider this zone, the larger the temperature drop ΔT. Figure 5 shows the reduction in the thermal slip length L_T evaluated at the hotter and colder interfaces with increasing ε_{LS} and decreasing σ_{LS}. The larger fluctuations in Fig. 5(c) stem from the larger noise-to-signal ratio of ΔT for $(T_{\rm source}, T_{\rm sink}) = (1.4, 1, 2)$ [54], as expected in cases subject to smaller temperature differentials $T_{\rm source} - T_{\rm sink}$. For the same reasons as mentioned above in regard to Fig. 4, here too the thermal slip length is not always larger at the colder L/S interface.

While historically physicists have always measured the degree of thermal impedance at a L/S interface using the thermal slip length, researchers throughout different engineering communities still prefer to use the thermal boundary resistance defined as $\mathcal{R} = \Delta T/J_z$. For this study, we found that the liquid (and solid) layers behave as Fourier media, for which the magnitude of the thermal flux is then given by $J_z = k|dT/dz|_{\rm liq}$, where k is the effective thermal conductivity and $|dT/dz|_{\rm liq}$ is a constant due to the linearity of the temperature profile $T_{\rm liq}(z)$. As a result, the thermal boundary resistance is related to the thermal slip length through the simple relation $\mathcal{R} = L_T/k$. Therefore, the data in Fig. 5, when multiplied by the factor k^{-1}, yield the corresponding curves for the thermal boundary resistance, which replicate the same behavior as in Fig. 5, except for the amplitude, and are therefore not reproduced here. The thermal conductivity values can be found in Ref. [54].

C. Influence of long-range translational order in the contact layer

Figures 6(a)–6(c) show the peak value of the in-plane structure factor $S^{\parallel}_{\rm max}$, which, all else being equal, is always larger for particles in the colder contact layer, as expected. Its magnitude increases with decreasing σ_{LS}, increasing ε_{LS}, and decreasing local temperature enforced by lower temperatures $T_{\rm sink}$. Of the 180 systems represented, there are six special cases for which the structure factor at $\varepsilon_{LS} = 1.0$ exceeds 0.8—namely, four cases with $T_{\rm sink} = 0.8$ and $\sigma = 0.8$, and two cases with $T_{\rm sink} = 1.0$ and $\sigma = 0.8$. (Additional information about these cases can be found in Ref. [54]). These cases also happen to exhibit near saturation in the values of $S^{\parallel}_{\rm max}$, due to strong binding with the solid lattice and the formation of a solidlike contact layer. By contrast, all the other data exhibit a steady increase in $S^{\parallel}_{\rm max}$ as ε_{LS} increases from 0.1 to 1.0. The topmost curve in Figs. 6(a)–6(c) also reveals an interesting structural transition for $\varepsilon_{LS} = 0.2$ and $\sigma_{LS} = 0.8$, marked by the dip in $S^{\parallel}_{\rm max}$ at $\varepsilon_{LS} = 0.2$. This system represents the most disordered state of runs conducted with the lowest $T_{\rm sink}$ (0.8) and the smallest σ_{LS} (0.8). This combination of input variables leads to a more frustrated configuration of particles in the contact layer less able to adjust to the order and periodicity of the nearby solid lattice.

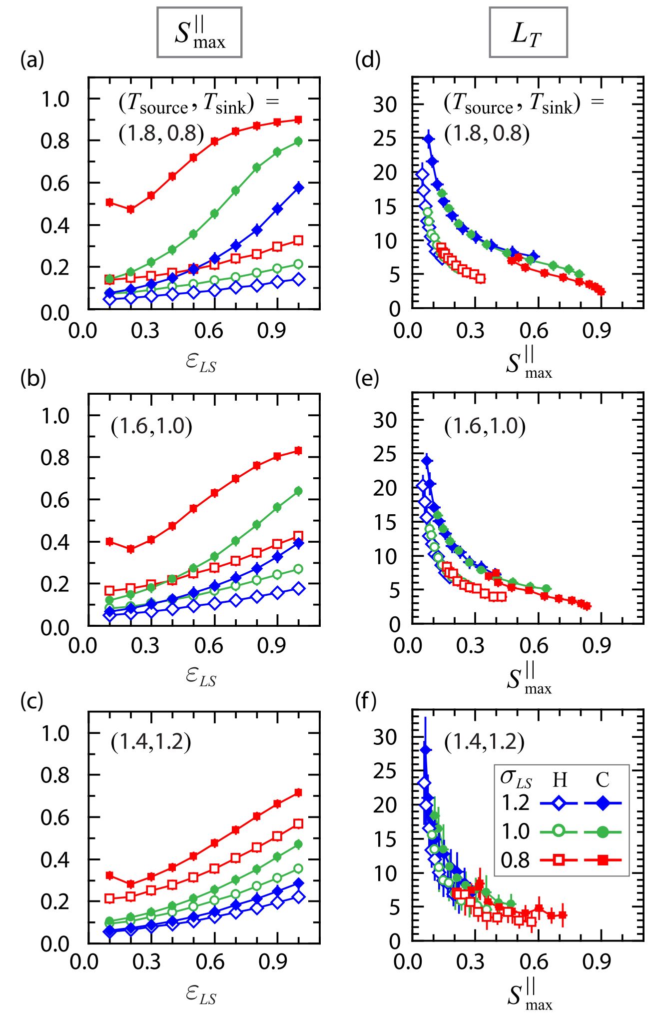

FIG. 6. (a)–(c) Increase in $S^{\parallel}_{\rm max}$ measured at the hotter (H) and colder (C) L/S interfaces for decreasing temperature ($T_{\rm source}$ or $T_{\rm sink}$), increasing ε_{LS}, or decreasing σ_{LS}. (The three exceptions are discussed further in the text.) Connector lines are a guide for the eye. (d)–(f) Reduction in thermal slip length L_T with increasing $S^{\parallel}_{\rm max}$.

D. Dependence of thermal slip length on long-range translational order in the contact layer

Figures 6(d)–6(f) show the reduction in the thermal slip length L_T with increasing $S^{\parallel}_{\rm max}$. This behavior reveals that a smaller thermal impedance is achieved when particles in the contact layer conform more closely to the order and periodicity of particles in the solid lattice. While this behavior is not unexpected, it is nonetheless interesting to note how rapid is the reduction in L_T with increasing $S^{\parallel}_{\rm max}$ and also how the data compress as the differential temperature $T_{\rm source} - T_{\rm sink}$ decreases. This behavior suggests the

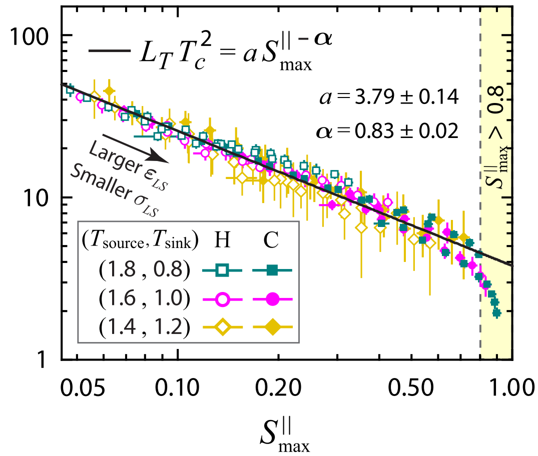

FIG. 7. Collapse of the data for the thermal slip length L_T vs the in-plane structure factor of the contact layer when scaled by the contact layer temperature T_c. The solid curve is the best fit to Eq. (10), excluding six points with $S_{max} > 0.8$ signifying solidlike behavior.

possibility of rescaling the data onto a master curve, as described next.

A nonlinear best fit to the power-law relation

$$L_T T_c^2 = a S_{max}^{-\alpha}. \tag{10}$$

was performed by orthogonal distance regression so as to incorporate standard deviations in the measured values of L_T, T_c, and $S_{max}^{||}$. The best fit, indicated by the superposed solid line in Fig. 7, yielded exponent $\alpha = 0.83 \pm 0.02$ and coefficient $a = 3.79 \pm 0.14$, where the values following the plus-or-minus sign denote 95% confidence levels. To confirm this was the best fit, we conducted regression tests by reducing the exponent of T_c from 2 to 1.5, which yielded $\alpha = 0.74 \pm 0.02$ and $a = 3.94 \pm 0.16$ and an increase in the residual sum of squares of about 20%. We also tried fitting the data with $\alpha = 1.0$ and allowing the exponent of T_c and the coefficient a to vary; the exponent then increased to 2.34 ± 0.12 and the coefficient reduced to 3.10 ± 0.11, with an increase in the residual sum of squares of more than 110%. Our allowing variation in all three fit constants, a, α, and the exponent of T_c, yielded a slight decrease in α from 0.83 ± 0.02 to 0.80 ± 0.03 and a decrease in the exponent of T_c from 2 to 1.83 ± 0.10. Assuming rational exponents then, the analysis suggests a scaling relation of the form

$$L_T \sim \frac{S_{max}^{||\,4/5}}{T_c{}^2}, \tag{11}$$

E. Dependence of thermal slip length on dominant vibrational frequencies in the contact zone

Given the master curve in L_T showing strong correlation with the order and periodicity of the contact layer as induced by the crystalline surface potential, we also examined the vibrational spectra of particles in the contact (liquid) layer and the first solid layer. In particular, we computed the vibrational density of states $\mathcal{D}(\nu)$ given by Eq. (9) for both layers and extracted the frequency ratio ν_S/ν_L, where ν_S and ν_L denote the frequencies corresponding to the respective maximum in the density of states. Figure 8(a) shows an example of the density of states for the solid and liquid layers for the colder L/S interface obtained with $(T_{source}, T_{sink}) = (1.6, 1.0)$, $\sigma = 1.0$, and $\varepsilon = 0.1$ and $\varepsilon = 1.0$. The data show that the density of states for the contact layer is more sensitive to the increase in ε_{LS} than is that for the solid layer, as is evident from the relatively larger shift in ν_L toward higher frequencies than occurs for ν_S.

As is well-known, $\mathcal{D}(\nu = 0)$ is proportional to the self-diffusion coefficient of liquid particles. For an isotropic classical fluid of identical particles of mass m at thermal equilibrium at temperature T, the expression for the self-diffusion coefficient (in dimensional units) is $D = (k_B T/12m)\mathcal{D}(\nu = 0)$ [52]. While this relation is no longer exact for particles near a solid surface because of anisotropic effects such as liquid layering, it is still the case that a smaller value of $\mathcal{D}(\nu = 0)$ indicates a smaller diffusion coefficient. We found that in systems at fixed values of (T_{source}, T_{sink}) and σ_{LS}, $\mathcal{D}(\nu = 0)$ decreased noticeably as ε_{LS} was increased from 0.1 to 1.0, as is evident in the example shown in Fig. 8(a). As expected, an increase in the bonding strength ε_{LS} hinders in-plane diffusion of liquid particles. A decrease in the in-plane mobility was also observed with colder contact layer temperatures T_c enforced by lower reservoir temperatures T_{sink}.

The data in Figs. 8(b)–8(d) show that smaller ratios ν_S/ν_L, indicative of stronger L/S vibrational coupling, are achieved with larger ε_{LS}, smaller σ_{LS}, and lower contact layer temperature achieved by lowering T_{source} or T_{sink}. The anomalous and large reduction in ν_S/ν_L observed for all (T_{source}, T_{sink}) pairs with $\varepsilon_{LS} = 0.1$ and $\sigma_{LS} = 0.8$ corresponds to those contact layers with $\nu_L \approx \nu_S/2$. Such behavior signifies the formation of a contact layer with superlattice symmetry, i.e., same symmetry as the [001] fcc solid facet but twice its lattice constant. Figure 9 shows the collapse of the data for the thermal slip length in terms of the dominant vibration frequencies in the L/S contact zone when scaled by the contact layer temperature and LJ interaction distance σ_{LS}. Clearly, the six cases just noted with contact layers resembling solidlike superlattices do not fit the general trend. The best fit to the data, indicated by the solid line, represents a nonlinear fit to the relation

$$L_T T_c^{3/2}/\sigma_{LS}^2 = b\left(\frac{\nu_S}{\nu_L}\right)^{\beta}, \tag{12}$$

obtained by orthogonal distance regression, which incorporates the standard deviations in the measured values of

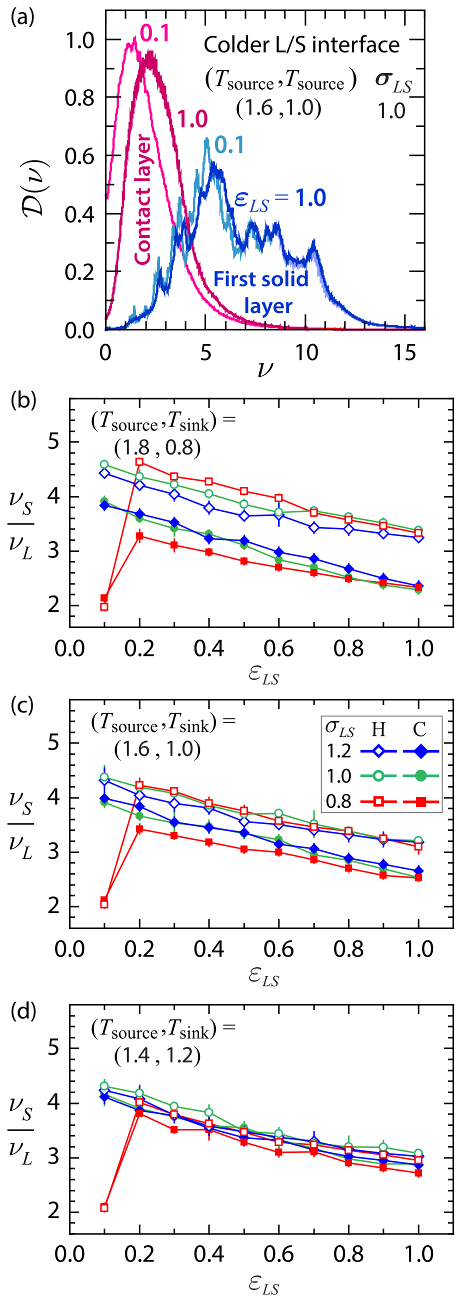

FIG. 8. (a) Vibrational frequency spectra per particle $\mathcal{D}(\nu)$ for the contact (liquid) layer and the first solid layer at the colder L/S interface for $(T_{\mathrm{source}}, T_{\mathrm{sink}}) = (1.6, 1.0)$, $\sigma_{LS} = 1.0$, and $\varepsilon_{LS} = 0.1$ and $\varepsilon_{LS} =$ 1.0. Frequencies ν_S and ν_L were extracted from maxima of $\mathcal{D}(\nu)$. (b)–(d) Reduction in the ratio ν_S/ν_L for increasing ε_{LS} and colder contact layers. (Anomalous behavior for six data points with $\varepsilon_{LS} = 0.1$ and $\sigma_{LS} = 0.8$ is discussed in the text.)

L_T, T_c, and ν_S/ν_L. The best fit yielded $\beta = 2.93 \pm 0.11$ and $b = 0.35 \pm 0.05$, where the values following the plus-or-minus sign denote 95% confidence levels. Expansion of the search to allow variation of all the variables shown resulted in little change to the exponent of σ_{LS}, a small increase in the exponent of T_c from 3/2 to 1.61 ± 0.13, and an

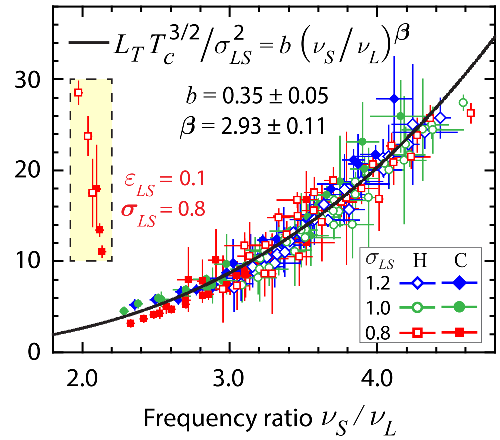

FIG. 9. Collapse of the data for the thermal slip length L_T vs the frequency ratio ν_S/ν_L when scaled by the contact layer temperature T_c and LJ interaction distance σ_{LS}. The solid curve is the best fit to Eq. (12). The fit excludes six data points for solid-like contact layers with superlattice symmetry, as described in the text.

even smaller increase in the exponent β from 2.93 ± 0.11 to 2.98 ± 0.14. Regression attempts based on third-order polynomials in ν_S/ν_L led to substantially worse fits no matter what the initial seed values were.

Assuming power-law behavior with rational exponents, the analysis for the thermal slip length behavior in the frequency domain suggests the scaling relation

$$L_T \sim \frac{\sigma_{LS}^2}{T_c^{3/2}} \left(\frac{\nu_S}{\nu_L}\right)^3. \tag{13}$$

IV. CONCLUSION

This computational study was designed to elicit the dependence of the thermal slip length on *correlated behavior* within the L/S contact zone comprising the first solid layer and the first liquid layer, i.e., contact layer. In particular, we focused on the long-range translational order and vibrational spectrum in the contact layer as influenced by the order and symmetry of the solid crystal. For the layered system used to examine the thermal transfer process, the input parameters were restricted to the temperatures of the Langevin source and sink reservoirs and the Lennard-Jones intermolecular parameters ε_{LS} and σ_{LS}. Different parameter sets naturally generated different values of the thermal flux propagating across the S/L/S system and different contact layer temperatures. Data were collected simultaneously from the hotter and colder L/S interfaces, yielding a total of 180 systems. The two quantities used to measure correlated behavior across the L/S interface were the peak value of the in-plane structure factor of the contact layer, which coincided with the smallest set of reciprocal lattice vectors of the fcc solid surface, and the ratio of frequencies defined by the maxima in the vibrational density of states of the first solid layer and the contact layer.

Excluding a handful of cases involving solidlike and not liquidlike contact layers, the data for the thermal slip length L_T versus structure factor, when scaled by a power of T_c, collapse nicely onto a master curve described by a simple power-law relation. Likewise, in the frequency domain, the data for L_T also undergo collapse onto a simple power-law equation when scaled by (different) powers of T_c and σ_{LS}. From the well-known property of corresponding states applicable to the Lennard-Jones potential, we anticipate similar power-law relations for other LJ systems so long as the fluid state is not near a critical or triple point. In future studies, it will be interesting to explore how more complex intermolecular potentials for L/S interactions modify these power-law relations.

The important take-away message from this work is not the numerical values of the fit constants but the fact that the thermal slip length is governed by power-law behavior stemming from the correlated spatial and frequency behavior in the L/S contact zone. More generally, these power-law relations underscore the critical role of *surface-localized phonons* in regulating thermal flux. While it has been known for decades that surface phonons from diffusive scattering at a rough interface are responsible for the fact that the thermal boundary resistance of a helium liquid/helium solid interface is much smaller [57] than the value predicted by the acoustic mismatch theory [6], we know of no such studies related to surface phonon localization in normal L/S interfaces.

On the experimental side, L/S interfaces pose many more challenges to measurement than S/S interfaces, and so validation of the relations reported in this work is likely not imminent. Perhaps high-resolution techniques combining small-angle neutron scattering with neutron reflectometry may be successful in extracting measurements of the in-plane static structure factor and vibrational spectrum of the contact layer for systems in thermal nonequilibrium. The more difficult challenge, which has persisted for decades, will be accurate measurement of the temperature drop in normal (i.e., nonsuperfluid) L/S systems, which may require new instrumentation. For these reasons, we still view particle-based simulations as the only viable high-resolution probe for quantifying the thermal boundary impedance of a normal L/S interface at this time.

ACKNOWLEDGMENTS

The authors gratefully acknowledge funding from a 2019 NASA Space Technology Research Fellowship (H.K.) and the generous assistance of Dr. Peter Thompson, information technology administrator of the LIS2T computing cluster used in this study.

Conceptualization: S.M.T.; Data curation: S.M.T.; Formal analysis: H.K. and S.M.T.; Funding acquisition: S.M.T.; Investigation: H.K. and S.M.T.; Methods: S.M.T.; Project administration: S.M.T.; Resources: S.M.T.; Software: H.K. and S.M.T.; Supervision: S.M.T.; Validation: H.K. and S.M.T; Visualization: H.K. and S.M.T.; Writing—original draft: S.M.T.; Writing—review and editing: S.M.T.

DATA AVAILABILITY

The data that support the findings of this article are openly available [54].

[1] R. van Erp, R. Soleimanzadeh, L. Nela, G. Kampitsis, and E. Matioli, Co-designing electronics with microfluidics for more sustainable cooling, Nature **585**, 211 (2020).
[2] G. Rak, IBM demos transistor built for liquid nitrogen cooling, https://spectrum.ieee.org/nanosheet-transistor (2023).
[3] S. Rangarajan, S. N. Schiffres, and B. Sammakia, A review of recent developments in “on-chip” embedded cooling technologies for heterogeneous integrated applications, Engineering **26**, 185 (2023).
[4] R. Saligram, A. Raychowdhury, and S. Datta, The future is frozen: Cryogenic CMOS for high-performance computing, Chip **3**, 100082 (2024).
[5] J. Liu, *Advanced Liquid Metal Cooling for Chip, Device and System* (World Scientific Publishing Co. Pte. Ltd., Singapore, 2022).
[6] I. M. Khalatnikov, Teploobmen mezhdu tverdym telom i Geliem-ii, Zh. Eksp. Teor. Fiz. **22**, 687 (1952).
[7] G. L. Pollack, Kapitza resistance, Rev. Mod. Phys. **41**, 48 (1969).
[8] E. T. Swartz and R. O. Pohl, Thermal boundary resistance, Rev. Mod. Phys. **61**, 605 (1989).
[9] C. L. M. H. Navier, Mémoire sur les lois du mouvement des fluides, Mémoires de l’Académie Royale des Sciences de l’Institut de France **6**, 389 (1823).
[10] P. A. Thompson and S. M. Troian, A general boundary condition for liquid flow at solid surfaces, Nature **389**, 360 (1997).
[11] P. A. Thompson and M. O. Robbins, Shear flow near solids: Epitaxial order and flow boundary conditions, Phys. Rev. A **41**, 6830 (1990).
[12] J.-L. Barrat and L. Bocquet, Infuence of wetting properties on hydrodynamic boundary conditions at a fluid/solid interface, Faraday Discuss. **112**, 119 (1999).
[13] N. V. Priezjev and S. M. Troian, Molecular origin and dynamic behavior of slip in sheared polymer films, Phys. Rev. Lett. **92**, 018302 (2004).
[14] N. V. Priezjev, A. A. Darhuber, and S. M. Troian, Slip behavior in liquid films on surfaces of patterned wettability: Comparison between continuum and molecular dynamics, Phys. Rev. E **71**, 041608 (2005).
[15] N. V. Priezjev and S. M. Troian, Influence of periodic wall roughness on the slip behaviour at liquid/solid interfaces: Molecular-scale simulations versus continuum predictions, J. Fluid Mech. **554**, 24 (2006).
[16] S. Matsumoto, Molecular dynamics simulation of a liquid droplet on a solid surface, J. Jap. Soc. Tribol. **42**, 93 (1997).

[17] S. Maruyama, T. Kurashige, S. Matsumoto, Y. Yamaguchi, and T. Kimura, Liquid droplet in contact with a solid surface, Microscale Thermophys. Eng. **2**, 49 (1998).
[18] T. Ohara and D. Suzuki, Intermolecular energy transfer at a solid–liquid interface, Microscale Thermophys. Eng. **4**, 189 (2000).
[19] J.-L. Barrat and F. Chiaruttini, Kapitza resistance at the liquid–solid interface, Mol. Phys. **101**, 1605 (2003).
[20] L. Xue, P. Keblinski, S. R. Phillpot, S. U.-S. Choi, and J. A. Eastman, Two regimes of thermal resistance at a liquid–solid interface, J. Chem. Phys. **118**, 337 (2003).
[21] M. Vuorio, Role of wetting and nanoscale roughness on thermal conductance at liquid–solid interface, Appl. Phys. Lett. **99**, 073112 (2011).
[22] S. Murad and I. K. Puri, Thermal transport across nanoscale solid–fluid interfaces, Appl. Phys. Lett. **92**, 133105 (2008).
[23] H. Han, S. Mérabia, and F. Müller-Plathe, Thermal transport at solid–liquid interfaces: High pressure facilitates heat flow through nonlocal liquid structuring, J. Phys. Chem. Lett. **8**, 1946 (2017).
[24] G. Balasubramanian, S. Banerjee, and I. K. Puri, Unsteady nanoscale thermal transport across a solid–fluid interface, J. Appl. Phys. **104**, 064306 (2008).
[25] A. K. M. M. Morshed, T. C. Paul, and J. A. Khan, Atomistic simulation of temperature dependent thermal transport across nanoconfined liquid, Physica E **47**, 246 (2013).
[26] T. Ohara and D. Torii, Molecular dynamics study of thermal phenomena in an ultrathin liquid film sheared between solid surfaces: The influence of the crystal plane on energy and momentum transfer at solid-liquid interfaces, J. Chem. Phys. **122**, 214717 (2005).
[27] D. Torii, T. Ohara, and K. Ishida, Molecular-scale mechanism of thermal resistance at the solid–liquid interfaces: Influence of interaction parameters between solid and liquid molecules, J. Heat Transfer **132**, 012402 (2010).
[28] H. Kaifu, S. M. Troian, and A. I. Baskin, How caged motion in the contact layer enhances thermal tunneling across a liquid/solid interface, Phys. Rev. Res. **6**, 033123 (2024).
[29] B. H. Kim, A. Beskok, and T. Cagin, Molecular dynamics simulations of thermal resistance at the liquid-solid interface, J. Chem. Phys. **129**, 174701 (2008).
[30] B. Ramos-Alvarado, S. Kumar, and G. P. Peterson, Solid–liquid thermal transport and its relationship with wettability and the interfacial liquid structure, J. Phys. Chem. Lett. **7**, 3497 (2016).
[31] C. U. Gonzalez-Valle, S. Kumar, and B. Ramos-Alvarado, Thermal transport across SiC-water interfaces, ACS Appl. Mater. Interfaces **10**, 29179 (2018).
[32] S. Li, Y. Chen, J. Zhao, C. Wang, and N. Wei, Atomic structure causing an obvious difference in thermal conductance at the Pd–H_2O interface: A molecular dynamics simulation, Nanoscale **12**, 17870 (2020).
[33] H. Heinz, R. A. Vaia, B. L. Farmer, and R. R. Naik, Accurate simulation of surfaces and interfaces of face-centered cubic metals using 12-6 and 9-6 Lennard-Jones potentials, J. Phys. Chem. C **112**, 17281 (2008).
[34] K. Kanhaiya, S. Kim, W. Im, and H. Heinz, Accurate simulation of surfaces and interfaces of ten FCC metals and steel using Lennard–Jones potentials, NPJ Comput. Mater. **7**, 17 (2021).
[35] E. Helfand and S. A. Rice, Principle of corresponding states for transport properties, J. Chem. Phys. **32**, 1642 (1960).
[36] S. Plimpton, Fast parallel algorithms for short-range molecular dynamics, J. Comput. Phys. **117**, 1 (1995).
[37] A. P. Thompson, H. M. Aktulga, R. Berger, D. S. Bolintineanu, W. M. Brown, P. S. Crozier, P. J. intVelde, A. Kohlmeyer, S. G. Moore, T. D. Nguyen, R. Shan, M. J. Stevens, J. Tranchida, C. Trott, and S. J. Plimpton, LAMMPS—A flexible simulation tool for particle-based materials modeling at the atomic, meso, and continuum scales, Comput. Phys. Commun. **271**, 108171 (2022).
[38] A. Michels, H. Wijker, and H. Wijker, Isotherms of argon between 0 °C and 150 °C and pressures up to 2900 atmospheres, Physica **XV**, 627 (1949).
[39] L. Verlet, Computer "experiments" on classical fluids. I. Thermodynamical properties of Lennard-Jones molecules, Phys. Rev. **159**, 98 (1967).
[40] B. L. Holian and D. J. Evans, Shear viscosities away from the melting line: A comparison of equilibrium and nonequilibrium molecular dynamics, J. Chem. Phys. **78**, 5147 (1983).
[41] M. Thol, G. Rutkai, A. Köster, R. Lustig, R. Span, and J. Vrabec, Equation of state for the Lennard-Jones fluid, J. Phys. Chem. Ref. Data **45**, 023101 (2016).
[42] M. Cieplak, J. Koplik, and J. R. Banavar, Boundary conditions at a fluid–solid interface, Phys. Rev. Lett. **86**, 803 (2001).
[43] J. H. Sikkenk, J. O. lndekeu, J. M. J. van Leeuwen, E. O. Vossnaek, and A. F. Bakker, Simulation of wetting and drying at solid–fluid interfaces on the Delft molecular dynamics processor, J. Stat. Phys. **52**, 23 (1988).
[44] A. Giri and P. E. Hopkins, Spectral analysis of thermal boundary conductance across solid/classical liquid interfaces: A molecular dynamics study, Appl. Phys. Lett. **105**, 033106 (2014).
[45] K. Sääskilahti, J. Oksanen, J. Tulkki, and S. Volz, Spectral mapping of heat transfer mechanisms at liquid-solid interfaces, Phys. Rev. E **93**, 052141 (2016).
[46] M. R. Hasan, T. Q. Vo, and B. Kim, Manipulating thermal resistance at the solid–fluid interface through monolayer deposition, RSC Adv. **9**, 4948 (2019).
[47] R. J. Stevens, L. V. Zhigilei, and P. M. Norris, Effects of temperature and disorder on thermal boundary conductance at solid–solid interfaces: Nonequilibrium molecular dynamics simulations, Int. J. Mech. Sci. **50**, 3977 (2007).
[48] Z. Liang and P. Keblinski, Finite-size effects on molecular dynamics interfacial thermal-resistance predictions, Phys. Rev. B **90**, 075411 (2014).
[49] W. G. Hoover, Canonical dynamics: Equilibrium phase-space distributions, Phys. Rev. A **31**, 1695 (1985).
[50] T. Schneider and E. Stoll, Molecular-dynamics study of a three-dimensional one-component model for distortive phase transitions, Phys. Rev. B **17**, 1302 (1978).
[51] In many studies of the L/S interface, the liquid structure factor is often computed from the relation $|\sum_p^{N_c}\exp(-i\mathbf{k}\cdot\mathbf{r}_p)|^2$, a simplification strictly valid for particles on sites of a Bravais lattice.
[52] P. H. Berens, D. H. J. Mackay, G. M. White, and K. R. Wilson, Thermodynamics and quantum corrections from

molecular dynamics for liquid water, J. Chem. Phys. **79**, 2375 (1983).

[53] S. T. Lin, M. Blanco, and W. A. Goddard, The two-phase model for calculating thermodynamic properties of liquids from molecular dynamics: Validation for the phase diagram of Lennard-Jones fluids, J. Chem. Phys. **119**, 11792 (2003).

[54] H. Kaifu and S. M. Troian, DataSets_PhysRevAppl_LX18512N.pdf, CaltechDATA, https://doi.org/10.22002/5atzb-v8e04 (2025).

[55] S. Murad and I. K. Puri, Molecular simulation of thermal transport across hydrophilic interfaces, Chem. Phys. Lett. **467**, 110 (2008).

[56] A. Pham, M. Barisik, and B. Kim, Pressure dependence of Kapitza resistance at gold/water and silicon/water interfaces, J. Chem. Phys. **139**, 244702 (2013).

[57] T. Nakayama, New channels of energy transfer across a solid-liquid He interface, J. Phys. C: Solid State Phys. **18**, L667 (1985).